Journal Pre-proof

Evaluating potential power output of terrestrial thermoradiative diodes with atmospheric modelling

Jamie A. Harrison, Phoebe M. Pearce, Fei Yang, Michael P. Nielsen, Helen E. Brindley, Nicholas J. Ekins-Daukes

PII: S2589-0042(24)02571-9

DOI: https://doi.org/10.1016/j.isci.2024.111346

Reference: ISCI 111346

To appear in: *ISCIENCE*

Received Date: 5 August 2024

Revised Date: 1 October 2024

Accepted Date: 5 November 2024

Please cite this article as: Harrison, J.A., Pearce, P.M., Yang, F., Nielsen, M.P., Brindley, H.E., Ekins-Daukes, N.J., Evaluating potential power output of terrestrial thermoradiative diodes with atmospheric modelling, *ISCIENCE* (2024), doi: https://doi.org/10.1016/j.isci.2024.111346.

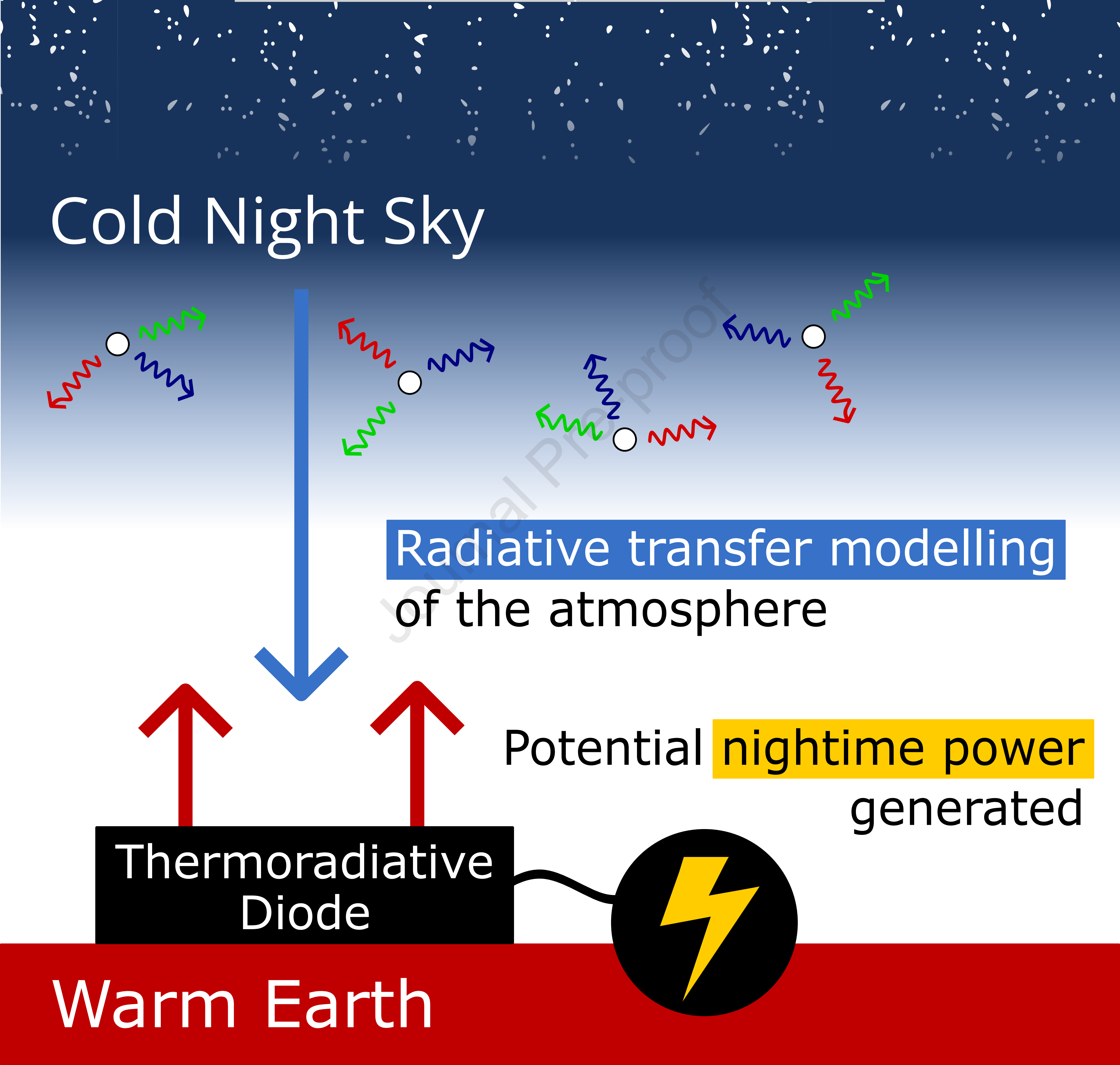
Cold Night Sky
Radiative transfer modelling
of the atmosphere
Potential nightime power
generated
Thermoradiative
Diode
Warm Earth

Evaluating potential power output of terrestrial thermoradiative diodes with atmospheric modelling

Jamie A. Harrison[1], Phoebe M. Pearce[1], Fei Yang[2], Michael P. Nielsen[1], Helen E. Brindley[2], and Nicholas J. Ekins-Daukes[1,3*]

[1]School of Photovoltaic and Renewable Energy Engineering, UNSW Sydney, Kensington, NSW 2052, Australia
[2]Department of Physics, Imperial College London, South Kensington SW7 2AZ, United Kingdom
[3]Lead contact
[*]Correspondence: nekins@unsw.edu.au

SUMMARY

A thermoradiative diode is a device that can generate power through thermal emission from the warm Earth to the cold night sky. Accurate assessment of the potential power output requires knowledge of the downwelling radiation from the atmosphere. Here, accurate modelling of this radiation is used alongside a detailed balance model of a diode at the Earth's surface temperature to evaluate its performance under nine different atmospheric conditions. In the radiative limit, these conditions yield power densities between 0.34 and 6.5 W.m^{-2}, with optimal bandgaps near 0.094 eV. Restricting the angles of emission and absorption to less than a full hemisphere can marginally increase the power output. Accounting for non-radiative processes, we suggest that if a 0.094 eV device would have radiative efficiencies more than two orders of magnitude lower than a diode with a bandgap near 0.25 eV, the higher bandgap material is preferred.

KEYWORDS

thermoradiative power, atmospheric modelling, radiative emission, mid-infrared emission, atmospheric downwelling

INTRODUCTION

In 2014, Byrnes et al. proposed several schemes by which the emission of infrared radiation from the Earth's warm surface into the cold sky can generate electrical power[1]. One proposed implementation of this concept is a low bandgap p-n junction, a thermoradiative diode (TRD), that produces current at small reverse biases through the emission of infrared photons. Figure 1a shows a simplified depiction of this mode of operation. Thermoradiative operation of HgCd(Zn)Te photodiodes has been demonstrated experimentally through the measurement of photocurrents[2 3] and of current-voltage (I-V) curves[4], with peak power densities on the order of mW.m^{-2}.[5]

Downwelling radiation received by a TRD on the Earth's surface, depicted by the blue arrow in Figure 1a, is a key factor determining the achievable power output from a TRD. The present work models this downwelling radiation using radiative transfer modelling of the atmosphere at various locations and times, as summarized in Figure 1b, in order to estimate power outputs for terrestrial TRDs.

TRDs occupy the opposite I-V quadrant to photovoltaic (PV) devices. The I-V shapes can be compared qualitatively in the radiative limit: a photovoltaic cell produces current when it absorbs more photons than it emits – as the operating voltage increases, the PV cell emission increases until open circuit, where the photogeneration (absorption) and radiative recombination (emission) rates cancel out and $I = 0$. A TRD produces current when it emits more photons than it absorbs – as the negative operating voltage increases in magnitude, the diode's emissions decrease until the photogeneration and radiative recombination rates cancel out. If the TRD operates in an environment where it receives significant downwelling radiation, the current decreases due to increased absorption and the V_{oc} reduces in magnitude – the "high downwelling" curve in Figure 1c illustrates this shift, showing the decrease in the power output at higher levels of downwelling radiation.

An application of detailed balance was undertaken by Strandberg[6] to establish efficiency limits for TRDs that are analogous to the Shockley-Queisser limit for photovoltaic cells. The operation of a TRD in the radiative limit as described by detailed balance is depicted in Figure 1d and stated in Eq. 13. To summarize, the number of emitted photons minus the number of absorbed photons gives the carrier generation and thus the current, and the voltage bias is given by the quasi-Fermi level splitting. By applying detailed balance, Santhanam and Fan[2] found a maximum power density of 54.8 $W.m^{-2}$ for emission from a TRD held at 300K to a blackbody 3K environment, which corresponds to a hypothetical and idealised case where a TRD on Earth can utilize outer space directly as a cold reservoir.

For non-ideal cases, estimations of the terrestrial performance of thermoradiative diodes typically model the environment as a blackbody with some effective temperature below that of the emitter[1 6 7], which provides an approximation of the radiative environment in the absence of realistic data. However, the particular spectral shape of atmospheric downwelling radiation is not accounted for in the smooth blackbody spectra, which complicates the process of estimating the true potential of terrestrial, thermoradiative power generation. When the spectral shape is considered, it is often through an "atmospheric transparency window" such as the one between 8 and 13 µm, which allows emitted radiation to access the cold of outer space. However, the language of optical "access to" outer space is useful for a limited set of clear-sky conditions with very low water vapour contents. Under real operating conditions, the atmosphere is neither fully opaque nor transparent.

Ono et al.[3] consider this variable transmissivity in their detailed balance analysis by calculating downwelling radiation as a weighed combination of emissions from a 298K atmosphere and a 3K universe. By varying the diode temperature for fixed atmospheric conditions, they find good correspondence between their model and measured photocurrents. However, for passive nighttime terrestrial power generation such as suggested in[1 7], operational TRDs would be subject to a variety of downwelling radiation profiles, which depend on the location and time.

Here, downwelling data obtained through line-by-line radiative transfer (LBLRT) modelling of the atmosphere for nine sample conditions is used with a detailed balance method to evaluate the performance of a terrestrial TRD in the radiative limit. Unlike PV, where peak efficiency corresponds to maximum power output, the peak efficiency and peak power points diverge significantly for TRDs[8 5]. As such, power density is used as the figure of merit throughout this work. The power output is shown to depend strongly on atmospheric water vapour content – which varies seasonally – and the optimal bandgap for an ideal device is identified at or around 0.094 eV, the start of the atmospheric transparency window, with a steep drop in performance away from this optimum. A simple analysis is conducted to show that extending the range of angles for emission and absorption beyond a certain range – around 60° for typical clear-sky conditions – has a limited impact on the output power density. Non-radiative processes, on the other hand, have a very significant impact on the power output and the optimal bandgap[4 8 9 10]. Due to the prominence of Auger processes in low-bandgap semiconductors, quantifying the effect of low radiative efficiencies allows more realistic estimates of possible power output.

RESULTS & DISCUSSION

Atmospheric modelling results

Atmospheric absorption increases the amount of downwelling infrared radiation received by the Earth's surface, reducing the effectiveness of a TRD device for power generation. Cloud and water vapour are the most effective absorbers – and conversely, most effective emitters – of infrared radiation in terms of their spectral coverage. Hence optimal conditions for TRD operation are under clear-skies with low water vapour concentrations. For the purposes of this manuscript we selected three locations, listed in Table 1. Based on the analysis of monthly-mean hourly resolution total column water vapour (TCWV) and cloud fields from the European Centre for Medium Range Weather Forecasts Reanalysis (ERA5)[11] all three locations show strong seasonality (Figure 2a) but have typically low TCWV and cloud cover during the winter months. For each location we extract days with low (winter) and medium and high (summer) nighttime TCWV values to illustrate the impact on the surface downwelling radiation. We assume that the chosen times are cloud and aerosol-free. We further assume that the TRD operates at the associated surface skin temperature, which is also available from the ERA5 archive. A summary of the cases is shown in Table 1. Figure 2b sets the TCWV for these cases in context by placing them against the distribution of hourly monthly mean values from 2010 to 2019 inclusive, over the range 60°N- 60°S.

The spectral photon flux density, $F_{\mathrm{ph}}(E_{\mathrm{ph}})$, as simulated using the Line-by-Line Radiative Transfer Model (LBLRTM) version 12.13[12], is shown in Figure 2d for the three Telfer scenarios (and in the supplemental information for all scenarios, in Figure S1). Details of the modelling are provided in the methods section. Increased atmospheric water vapour translates to an increased downwelling photon flux in the main atmospheric window between 0.09 and 0.16 eV. Lower humidities translate to a more transparent window although it is still inaccurate to treat the atmosphere as fully transparent across this range. At the lowest humidities an additional "dirty" window begins to open between 0.05 and 0.07 eV. In addition, further regions of moderately high transmission exist between 0.25-0.27 eV and 0.32-0.36 eV. In more opaque spectral regions the shape of the flux density follows that which would be expected from blackbody emission from near-surface atmospheric layers, whose emitting temperatures are strongly coupled to the skin temperature.

Optimal bandgap and power output in the radiative limit

Figure 3a compares the maximum power density achievable for a TRD at a range of bandgaps in the radiative limit. It compares the results obtained using the three modelled Telfer datasets (solid lines) to an effective temperature approximation (dashed lines). The effective temperature is calculated by matching the dataset to a blackbody spectrum with the same integrated downwelling power density, using the Stefan-Boltzmann law – details of this calculation are provided in the methods (Eq. 7 and Eq. 8). The black dotted line corresponds to an ideal case, where a TRD held at 300K emits into an environment modelled as a 3K blackbody, corresponding to emission into deep space. The peak power for this case is 54.8 W.m^{-2}, which matches the results from Santhanam et al.[2] and is achieved at bandgaps below 0.003 eV.

As shown in the plot, the effective temperature approximation does not account for the particular spectral shape of the downwelling flux. It noticeably underestimates the power densities possible near the start of the higher transmissivity spectral region. This underestimation is particularly notable for the 'Telfer mid' dataset, which has a limiting power density an order of magnitude larger than would be predicted from its corresponding effective temperature. Its effective temperature makes it seem comparable to the 'Telfer high' case, but the spectral distribution of the downwelling radiation in the mid-TCWV case enables significantly higher power outputs. Furthermore, the effective temperature approximation places the optimal bandgap near 0.04 eV, much lower than the results using downwelling spectra obtained through LBLRT modelling.

Figure 3b shows the maximum power densities for all the downwelling datasets listed in Table 1 (excluding the 3K BB reference). These power densities are calculated in the radiative limit, with an optimal bandgap and optimal operating voltage. At 6.5 $W.m^{-2}$, the 'Telfer low' conditions produce the largest power density because they combine a low humidity (low downwelling flux) with a high emitter temperature (high emitted flux) – see Figure 2c. The 'Telfer high' conditions, with their unusually high humidity (Figure 2b), produce the lowest power density at 0.34 $W.m^{-2}$. The order of magnitude spread in values for the same location highlights the sensitivity of the power output to atmospheric conditions. For the sampled conditions in other locations the spread is smaller, with the low TCWV case performing just over twice as well as the high TCWV case in Fresno and just over three times as well in Tamanrasset.

Figure 3b also indicates that $E_g = 0.094$ eV is the optimal bandgap for the range of realistic conditions sampled here (from 2 - 40 mm TCWV). As might be expected, this bandgap falls within the atmospheric window, as highlighted by the spectral photon flux for the 'Telfer low' case plotted in the background of Figure 3a. These results match the optimal bandgap of 0.094 eV (13.2 µm) identified in[3], which was calculated using detailed balance for a particular ambient temperature (293K) and using a particular atmospheric transmittance spectrum. At particularly high humidities – as the 'Telfer high' case here – the optimal bandgap shifts slightly to just over 0.1 eV, but these conditions appear relatively rarely (Figure 2b). Current density and power curves as a function of operating voltage for the three Telfer conditions, at the optimal bandgaps for each condition, are plotted in Figure 4.

Angular restriction

The power densities reported above consider a planar TRD perfectly emitting across a full hemisphere and, conversely, perfectly absorbing downwelling radiation across a full hemisphere. The atmospheric modelling results are defined per zenith angle, so they can be used to consider restrictions to the angles of emission and absorption. Here, we consider a simple case for angular restriction where, similar to the abrupt bandgap model, emission and absorption are 100% efficient within some cone defined by a cutoff zenith angle θ_c, and 0% efficient outside of this cone. A schematic of this model is shown in the inset of Figure 5. No assumptions are made here about the optics required to achieve this.

The cutoff angle is swept from a very narrow cone with $\theta_c = 10°$ to a full hemisphere $\theta_c = 90°$ (equivalent to the results in Figure 3). The relative change in the achievable power density, in the radiative limit, is shown in Figure 5 for the three Telfer datasets. The bandgap is fixed at its optimum for each given dataset, but the operating voltage V is optimized for each point. Enabling angular restriction did not impact the optimal bandgap and had minimal impact on the optimal operating voltage.

From Figure 5, some increase in output power is possible for the mid and high humidity conditions if the angles of emission are restricted. However, this enhancement is less than 10% for even the highest humidity case. Conversely, the plot shows that there is a window of relative insensitivity to cutoff angle, the size of which depends on the conditions. For the 'Telfer mid' case, for example, any cutoff angle between 60 and 90 degrees would output roughly the same power (±5%) as the full hemisphere case. This indicates that under common terrestrial operating conditions, increasing the emission cone beyond 60° provides diminishing returns.

Non-ideal radiative efficiencies

The low bandgaps which give the highest power output in the radiative limit are in practice strongly affected by intrinsic Auger processes, which limit the achievable power densities. In order to provide estimates of realistic power densities for terrestrial TRDs, non-radiative processes are included in this section. The fraction of total carrier recombination attributed to radiative recombination is quantified through the external radiative efficiency, η_{ext} (see Eq. 15), which is treated as a property of a given diode[5]. In an ideal case where the only generation and recombination pathways are radiative, $\eta_{\text{ext}} = 100\%$. As η_{ext} decreases, the prominence of non-radiative processes increases and output power density decreases.

Figure 6a shows the maximum power density as a function of two diode properties: bandgap and radiative efficiency. Power is expected to scale roughly linearly with radiative efficiency[38], so the constant power density contour lines have the same shape as the solid lines in Figure 3a, which correspond to $\eta_{\text{ext}} = 100\%$. The plot is only shown for the 'Telfer mid' case, but similar plots can be drawn for the other cases with very similar results.

Three bandgap and radiative efficiency combinations are selected as example diodes to compare across modelled conditions. The first case, diode A, is an ideal diode with a bandgap of $E_{\text{g}} = 0.094$ eV and $\eta_{\text{ext}} = 100\%$. The second case, diode B, keeps the optimal bandgap of $E_{\text{g}} = 0.094$ eV, with a radiative efficiency of $\eta_{\text{ext}} = 1\%$. As radiative efficiency is expected to increase with the bandgap, a third diode, diode C, is selected with $E_{\text{g}} = 0.25$ eV and $\eta_{\text{ext}} = 10\%$: a larger, less optimal bandgap but higher radiative efficiency. This third combination corresponds more closely to the mid-infrared HgCdTe diodes used by Nielsen et al.[4], which have nominal bandgaps between 0.22 and 0.31 eV and estimated radiative efficiencies between 0.8 and 6.5%. The three sample diodes are identified on the heatmap in Figure 6a. The power densities calculated for these diodes for all modelled conditions listed in Table 1 are shown in the scatter plot in Figure 6b.

From Figure 6b, under most conditions, diode B (ideal bandgap, 1% radiative efficiency) yields power densities roughly an order of magnitude larger than diode C (larger bandgap, 10% efficiency). Given power density is expected to scale approximately linearly with radiative efficiency[38], a 0.1% radiatively efficient diode with an ideal 0.094 eV bandgap would perform roughly the same as a 0.25 eV bandgap, 10% efficient diode. Therefore, if the realization of a material with an ideal, low bandgap is only possible with radiative efficiencies more than two orders of magnitude lower than a diode with a bandgap near 0.25 eV, it is likely more beneficial to use higher bandgap materials with better radiative efficiencies. Additionally, the TRD power output varies less across modelled conditions for diode C, and is less sensitive to TCWV (x-axis). Currently, commercial HgCdTe and III-V photodiodes can reach peak responsivities down to 0.116 eV – further research on diode fabrication with these materials might enable TRDs with low (near 0.094 eV) bandgaps, but the power output possible from such diodes will only increase if the lower bandgaps can be obtained with a less than two order of magnitude decrease in radiative efficiency.

Ultimately, however, the power outputs of terrestrial TRDs remain quite low, even with an ideal bandgap. The annotations on the right of Figure 6b map the detailed balance power densities to the power consumption of some typical household items, for context. A 12.3 m^2 area of solar panels can on an average day supply the power needs of an average residential customer is Sydney in 2023 (9.6 kWh daily[13]). This device area is multiplied by the TRD power density to compare what an equivalent area of TRD could power. The reference yearly average power density for solar PV is estimated using NREL's PVWatts calculator with the default settings in Sydney, which gives an annual yield of 1499 kWh/kW_{p}. With the PVWatts standard module efficiency of 19%, this translates into a yearly average power density of 32.5 kW.m^{-2}.

The mapping very optimistically assumes that the power output of the TRD is maintained over 24h to obtain some corresponding produced energy – this ignores the additional incoming radiation from the Sun during the day and is therefore not intended as a feasible energy generation estimate, but rather as a means of gaining a more intuitive understanding of the scale of power densities reported. A realistic estimate for solar PV can meet the daily energy needs of a customer in Sydney; a hypothetical equivalent area of a TRD with an optimal bandgap (diode B) could power a 5W phone charger for 2h. In the unrealistic case where non-radiative processes are completely ignored, a TRD could power a 60W fridge. It is important to note that the yearly average solar estimate includes nighttime in the 24h power production and accounts for many non-ideal system level effects which are ignored in the TRD calculations.

Limitations of the study

The detailed balance method used here is deliberately simple and models spectral and angular response as step functions (i.e. perfectly abrupt bandgap, perfectly abrupt angular cutoff allowing up to a full hemisphere of view). Realistic devices would have more gradual onsets to absorption and emission, and would require more complicated methods to accurately optically simulate (see, for example, ray tracing performed to model outcoupling from a hyperhemispherical lens by Nielsen et al.[4]). Additionally, this work has restricted the TRD emitter temperature to the Earth's skin temperature (surface temperature) for each condition sampled. Decoupling emitter temperature from atmospheric conditions, such that dry winter skies might be coupled with warm emitters utilizing waste heat, could enable limiting power densities beyond what is reported here. The scope of this study was deliberately limited, but further work could explore more complicated optical models and emitter temperature/atmospheric condition pairings.

Supplemental information index

PDF containing:

- Figures S1-S4 and their legends, which include plots of the atmospheric modelling results for all 9 sampled conditions and graphs supporting the methodological details provided.
- Table S1, summarizing the atmospheric modelling parameters described here in table format, and references associated to these parameters.

Acknowledgments

N.J.E.-D.is supported by the UNSW SHARP program, M.P.N. is supported by the UNSW Scientia Program, and P.M.P. is supported by a Research Fellowship from the ARC Centre of Excellence for Exciton Science CE170100026. J.A.H. is supported by Airbus Defence and Space. F.Y. was supported by Blackett Laboratory, Department of Physics, Imperial College London through the University Research Opportunities Programme (UROP).

Author contributions

N.J.E-D. conceived the project. F.Y. and H.E.B. designed the methodology for and performed the atmospheric modelling. J.A.H. developed the code to perform detailed balance calculation, with guidance from P.M.P, and analyzed the results. P.M.P., M.P.N., H.E.B, and N.J.E-D. supervised the project. J.A.H. created the visuals and wrote the manuscript, with contributions from H.E.B. for the atmospheric modelling methodology. All authors reviewed the manuscript.

Declaration of interests

The authors declare no competing interests.

MAIN FIGURE TITLES AND LEGENDS

Figure 1: Thermoradiative diode operation. a) A terrestrial TRD generates current by emitting thermal radiation from the warm Earth's surface to a colder sky. b) Atmospheric temperature and gas profiles corresponding to sample locations and times are inputted to the Line-by-Line Radiative Transfer Model (LBLRTM)[12] to estimate the downwelling spectral radiance as a function of wavenumber, $L_e(\tilde{v})$, at the Earth's surface from the cold sky as a function of viewing zenith angle, θ. c) Example I-V curves are drawn for TRDs, showing an ideal case with low downwelling radiation (such as a TRD operating in outer space) and a more realistic terrestrial operating case with high downwelling radiation. The quadrant for TRD operation here is defined by negative voltage and positive current. d) Schematic description of the detailed balance model used to estimate the TRD's power output in this work. The diagram shows the model in the radiative limit. As electrons leave the conduction band through the emission of a photon, electrons are drawn in from the external circuit to replenish the population (recombination current, shown with red arrows at the rightmost contact). If some electrons are promoted to the conduction band through absorption, the absorption current opposes the recombination current (blue arrow) and reduces the number of external electrons required to replenish the population. If the photons emitted outnumber the photons absorbed, positive current flows, with reverse bias.

Figure 2: Conditions selected for atmospheric modelling. a) Map of mean total column water vapour (TCWV) between 2000 and 2019 for January, UTC 0000 and June, UTC 0000 (averaged across the month and years). The three locations selected are identified. b) Histogram of hourly-monthly mean TCWV from 2010 to 2019 and for latitudes between 60S-60N (inclusive), annotated to indicate conditions modelled. c) Skin temperature vs TCWV for conditions modelled. d) Full-hemisphere downwelling photon flux density, modelled for the three Telfer conditions.

Figure 3: Power densities in the radiative limit. a) Maximum power density vs. bandgap in the radiative limit. Solid curves use modelling results (as shown in Figure 2d) to quantify downwelling radiation. Dashed curves use a blackbody environment at an "effective" temperature, calculated as 273.13K (low), 292.83K (mid), and 293.55K (high). Skin temperature is taken as the emitter temperature for all cases except the 3K blackbody environment, where it is set to 300K. Star and dots identify the optimal bandgaps. The spectral photon flux density corresponding to the 'Telfer low' case is plotted in light grey in the background for reference. b) Scatter plot of optimal bandgap and corresponding maximum power densities in the radiative limit for all modelled conditions, as identified in Table 1 (excluding the 3K BB case).

Figure 4: Current density and power density as a function of operating voltage, calculated for the three Telfer datasets, in the radiative limit and at the optimal bandgaps for each condition (0.094, 0.094, and 0.101 eV for low, mid, and high).

Figure 5: Restricting angles of emission and absorption, in the radiative limit. Relative change in max power density with cutoff angle, θ_c, compared to a full hemisphere. Bandgap E_g is fixed at the optimum for each dataset, and operating voltage V is optimized for each cutoff angle. The inset diagram illustrates the implementation of the cutoff angle, where 90° corresponds to a full hemisphere of emission and absorption.

Figure 6: Introducing non-radiative processes with radiative efficiencies below 100%. a) Power density from TRD as a function of bandgap and radiative efficiency for the 'Telfer mid' dataset. Each point represents an optimization over V, using Eq 16. Contour lines show constant power densities in [W.m^2]. Filled, half filled, and empty circles identify sample diodes A, B, and C, respectively. b) Scatter plot of power densities for the three sample diodes, for all the modelled conditions listed in Table 1. The conditions are listed in Table 1 and are consistent with the legend in Figure 3b. Annotations on the right contextualize the power densities by listing examples of what the energy produced over 24h could power.

MAIN TABLES, INCLUDING TITLES AND LEGENDS

Table 1: Atmospheric conditions modelled for this work.

STAR METHODS

Resource availability

Lead contact

Requests for further information or resources should be directed to the lead contact, Nicholas J. Ekins-Daukes (nekinsunsw.edu.au).

Materials availability

This study did not generate new materials.

Data and code availability

1. Data: The AER line file v3.8.1 database[14], the ERA5 database[11], and the US standard atmosphere[15] were used for atmospheric modelling. The atmospheric modelling results produced are published on Zenodo[16].

2. Code: The LBLRTM code v12.13[12] and MT_CKD v3.6[17] were used for atmospheric modelling. The code written specifically to perform and analyze all detailed balance calculations reported in this work is published on Zenodo[16].

3. Any additional information required to reanalyse the data reported in this paper is available from the lead contact upon request.

Method details

Atmospheric modelling

As shown in Figure 1c, the modelling of atmospheric radiation makes use of the LBLRTM code. Accounting for line-broadening and mixing effects, the code essentially solves Schwarzchild's equation of radiative transfer given an input atmospheric profile and appropriate boundary conditions to output either spectral transmission or directional radiance. In this case the initial boundary is cold space and the radiation propagates downwards to the Earth's surface. The angle of propagation is configurable: to enable the calculation of flux we simulate a number of upward zenith angles from vertically overhead (0°) to almost the horizon (85°). For the angular restriction calculations in particular, the three Telfer conditions were modelled at 0, 10, 20, 30, 40, 53, 60, 65, 70, 75, 80, and 85 degrees.

The code considers every individual absorption line for a set of user defined gases, with spectroscopic line parameters taken from the AER line file v3.8.1, which itself uses, as a baseline, input from HITRAN[18 19]. Water vapour continuum absorption is treated following the MT_CKD v3.6 parameterization[17]. Absorption due to 'heavy molecules' such as chlorofluorocarbons (CFCs) can be included via their absorption cross-sections. In our simulations we include the effects of H_2O, CO_2, O_3, CH_4, N_2O, CO, CFC-11, CFC-12, CCl_4, $CHClF_2$ and CF_4. Temperature, humidity and ozone profiles as a function of atmospheric pressure are taken from ERA5 for the times, dates and locations identified in Table 1. The remaining gases have a vertical profile which follows that provided by the US standard atmosphere[20] but with concentrations appropriate to 2023.

Surface downwelling radiances, $L_e(\tilde{v})$ (in W.m^{-2}.sr^{-1}/cm^{-1}) are output at a spectral resolution of approximately 0.0002 cm^{-1} before being averaged to increments of 0.5 cm^{-1} (6.2×10^{-5} eV), spanning from $\tilde{v} = 100.25$ cm^{-1} ($E_{\mathrm{ph}} = 0.012$ eV) to $\tilde{v} = 5499.75$ cm^{-1} ($E_{\mathrm{ph}} = 0.682$ eV).

Absorption from atmosphere

The $L_e(\tilde{v})$ downwelling radiance arrays produced by atmospheric modelling are converted to photon energy and photon flux, $L_{\mathrm{ph}}(E_{\mathrm{ph}})$, which are used to calculate the absorption of a planar TRD on Earth. For incident radiation across a full hemisphere (i.e. everywhere except in the Angular Restriction section), the diffusivity approximation can be used to estimate spectral irradiance from spectral radiance. To convert from directional spectral photon flux density L_{ph} [$\mathrm{s^{-1}.m^{-2}.sr^{-1}/eV}$] to spectral photon flux density F_{ph} [$\mathrm{s^{-1}.m^{-2}/eV}$] assuming downwelling across the hemisphere, we have:

$$F_{\mathrm{ph}}(E_{\mathrm{ph}}) = L_{\mathrm{ph}}(E_{\mathrm{ph}}, \theta = 53^\circ) \times \pi \tag{1}$$

For the angularly restricted calculations reported, L_{ph} is interpolated and extrapolated for any arbitrary θ between 0 and 90° from a finite set of modelled θ angles. Integrating L_{ph} over solid angle Ω (with $d\Omega = \sin\theta \, d\theta \, d\phi$) the spectral photon flux density is:

$$F_{\mathrm{ph}}(E_{\mathrm{ph}}, \theta_c) = 2\pi \int_0^{\theta_c} L_{\mathrm{ph}}(E_{\mathrm{ph}}, \theta) \, \cos\theta \, \sin\theta \, d\theta \tag{2}$$

with a factor 2π from integration over ϕ, the azimuth angle, and a $\cos\theta$ from assuming a Lambertian distribution over θ.

LBLRTM calculations were performed for 12 zenith angles between 0 and 85°. A path length approximation is used to interpolate between and extrapolate beyond modelled angles: $L_{\mathrm{ph}}(E_{\mathrm{ph}}, \theta)$ is taken to vary linearly with $\frac{1}{\cos\theta}$ (see the diagram in Figure S2 of the supplemental).

$$L_{\mathrm{ph}}(E_{\mathrm{ph}}, \theta) = m(E_{\mathrm{ph}}) \left(\frac{1}{\cos\theta}\right) + L_{\mathrm{ph}}(E_{\mathrm{ph}}, 0) \tag{3}$$

For any angle θ between the modelled θ_1 and θ_2:

$$L_{\mathrm{ph}}(E_{\mathrm{ph}}, \theta) = \left(\frac{L_{\mathrm{ph}}(E_{\mathrm{ph}}, \theta_2) - L_{\mathrm{ph}}(E_{\mathrm{ph}}, \theta_1)}{1/\cos\theta_2 - 1/\cos\theta_1}\right)(1/\cos\theta - 1/\cos\theta_1) + L_{\mathrm{ph}}(E_{\mathrm{ph}}, \theta_1) \tag{4}$$

In the extrapolation, as $\theta \to 90^\circ$, $L_{\mathrm{ph}}(\theta)$ becomes nonphysically large. The $\cos\theta$ factor is included in the interpolation to avoid numerical errors at oblique incidence angles.

$$L_{\mathrm{ph}}(E_{\mathrm{ph}}, \theta) \, \cos\theta = (L_{\mathrm{ph}}(E_{\mathrm{ph}}, \theta_2) - L_{\mathrm{ph}}(E_{\mathrm{ph}}, \theta_1)) \left(\frac{1 - \cos\theta/\cos\theta_1}{1/\cos\theta_2 - 1/\cos\theta_1}\right) + L_{\mathrm{ph}}(E_{\mathrm{ph}}, \theta_1) \, \cos\theta \tag{5}$$

For θ larger than any angle for which modelling data is available, Eq. 5 is used with the two largest known angles to extrapolate. In any case, at large angles, $(L_{\mathrm{ph}}(E_{\mathrm{ph}}, \theta) \cos\theta)$ tends to 0. The multiplier in the large brackets is constant for a given angle, whereas the other terms have some spectral dependence.

The integral over θ in Eq. 2 is performed by interpolating $(L_{\mathrm{ph}}(E_{\mathrm{ph}}, \theta) \cos\theta)$ from θ=0 to 90° in steps of 0.1° using Eq. 5, then numerically integrating this pre-interpolated 2D array (with axes θ and E_{ph}). This interpolation pre-sampling is used to speed up the optimization over V, which is performed at each point in Figure 5. Example plots of $L_{\mathrm{ph}}(E_{\mathrm{ph}}, \theta)$ and of $(L_{\mathrm{ph}}(E_{\mathrm{ph}}, \theta) \cos\theta)$ as interpolated using Eq. 5 are shown in the supplemental information (Figure S3).

In either case (full hemisphere with Eq. 1 or angularly restricted with Eq. 2), the photon density flux [$\mathrm{s^{-1}.m^{-2}}$] absorbed by a TRD with bandgap E_g is given by:

$$\dot{N}_{\mathrm{abs}}(E_g) = \int_{E_g}^{\infty} F_{\mathrm{ph}}(E_{\mathrm{ph}}) \, dE_{\mathrm{ph}} \tag{6}$$

which assumes 100% absorption of downwelling photons with energies E_{ph} larger than E_g and 0% absorption of photons below E_g. As modelling results are obtained at discrete photon energies, this integral is performed numerically using the trapezoidal method. Downwelling radiance is modelled up to $E_{\text{ph}} = 0.682$ eV, which therefore becomes the upper bound of the integral. The nighttime downwelling photon flux continues to diminish at higher photon energies such that the limited upper bound does not affect the power densities calculated up to the $E_g = 0.3$ eV reported in this (see "Sensitivity to finite spectral range" below for the check performed).

Where an effective sky temperature is used, the full hemisphere generalized Planck's equation is used for F_{ph}, as given in Eq. 11. The effective temperature T_{eff} corresponding to the modelled atmospheric conditions, which is inputted to Eq. 11, is calculated from the downwelling spectral irradiance, F_e, of the modelling data using the Stefan-Boltzmann law.

$$T_{\text{eff}} = \left[\frac{\int_0^\infty F_e(E_{\text{ph}})\, dE_{\text{ph}}}{\sigma}\right]^{\frac{1}{4}} \tag{7}$$

Because F_e is not defined to $E_{\text{ph}} = 0$, the integral is numerically calculated in parts, with the lower energies using a blackbody at the skin temperature, T_{skin}. With E_0 and E_f the lowest and highest photon energies for which modelling data exists:

$$T_{\text{eff}} = \left[\frac{1}{\sigma}\left(\int_0^{E_0} F_{e\,\text{BB}}(E_{\text{ph}}, T_{\text{skin}})\, dE_{\text{ph}} + \int_{E_0}^{E_f} F_e(E_{\text{ph}})\, dE_{\text{ph}}\right)\right]^{\frac{1}{4}} \tag{8}$$

The blackbody spectral irradiance, $F_{e\,\text{BB}}$, is Eq. 11 with $\mu = 0$ and converted from photon flux density to power density.

Emission from TRD

The directional and spectral photon flux density, L_{ph}, emitted from a TRD at temperature T [K] is estimated using the generalized Planck's equation

$$L_{\text{ph GP}}(E_{\text{ph}}, \mu, T) = \frac{2}{c^2(h/q)^3}\,\frac{E_{\text{ph}}^2}{\exp\left(\frac{E_{\text{ph}}-\mu}{kT/q}\right) - 1} \tag{9}$$

where μ is the quasi-Fermi level splitting, which is negative for TRD operation. As μ is given in [eV], the operating voltage is taken as $V = \mu$. A larger negative bias corresponds to a larger-magnitude negative μ and therefore to a lower emitted photon flux, which introduces the current-voltage tradeoff shown in Figure 1b.

To obtain the spectral photon flux density, F_{ph}, we assume a Lambertian distribution of radiation emitted from the TRD surface. From the same integration as Eq. 2, which can be solved analytically here because $L_{\text{ph GP}}$ is not a function of θ, the spectral photon flux density is:

$$\begin{aligned} F_{\text{ph GP}}(E_{\text{ph}}, \mu, T, \theta_c) &= 2\pi\, L_{\text{ph GP}}(E_{\text{ph}}, \mu, T) \int_0^{\theta_c} \cos\theta\, \sin\theta\, d\theta \\ &= 2\pi\, L_{\text{ph GP}}(E_{\text{ph}}, \mu, T)\, \sin^2\theta_c \end{aligned} \tag{10}$$

For a full hemisphere of emission, $\theta_c = 90$, which gives:

$$F_{\text{ph GP}}(E_{\text{ph}}, \mu, T) = \frac{2\pi}{c^2(h/q)^3}\,\frac{E_{\text{ph}}^2}{\exp\left(\frac{E_{\text{ph}}-\mu}{kT/q}\right) - 1} \tag{11}$$

The photon density flux emitted by a TRD with a bandgap E_g and operating at a voltage V is given by:

$$\dot{N}_{\text{emit}}(E_g, V, T) = \int_{E_g}^{\infty} F_{\text{ph GP}}(E_{\text{ph}}, \mu = V, T)\, dE_{\text{ph}} \tag{12}$$

This integral is performed numerically using the quad integration method implemented in SciPy.

Power density from detailed balance

For a given set of conditions, where the emitter temperature is fixed at T_{skin} and the downwelling photon flux density is calculated from modelling results, the current density can be calculated from a given bandgap and operating voltage as:

$$J(V, E_g) = q\left[\dot{N}_{\text{emit}}(E_g, V, T_{\text{skin}}) - \dot{N}_{\text{abs}}(E_g)\right] \tag{13}$$

This expression assumes that carrier pairs are only generated through the absorption of a photon, which occurs at a rate $\dot{N}_{\text{abs}}$, and can only recombine through the emission of a photon, which occurs at a rate $\dot{N}_{\text{emit}}$. Net recombined carriers are assumed to convert to inflowing current with 100% efficiency, so the net difference between photons emitted and photons absorbed is the number of carriers constituting the generated current. The current density, J, as defined here is positive for TRD operation, where the number of photons emitted exceeds the number absorbed (following the convention from Figure 1 and Pusch et al.[8]). Power density is calculated as $\mid JV \mid$ – the absolute value is taken because $V < 0$ and $I > 0$ here.

With the addition of non-radiative generation, G_{nr}, and recombination, R_{nr}, Eq. 13 becomes

$$J(V, E_g) = q\left[\dot{N}_{\text{emit}}(E_g, V, T_{\text{skin}}) - \dot{N}_{\text{abs}}(E_g) + R_{\text{nr}}(V) - G_{\text{nr}}(V)\right] \tag{14}$$

Following the derivation by Pusch et al.[8], the non-radiative recombination is quantified through the external luminescent efficiency, η_{ext}:

$$\eta_{\text{ext}} = \frac{\dot{N}_{\text{emit}}(V)}{\dot{N}_{\text{emit}}(V) + R_{\text{nr}}(V)} \tag{15}$$

which is taken to be constant for a given diode, i.e. independent of bias. The bias dependence of G_{nr} is ignored, and is approximated as $G_{\text{nr}} = R_{\text{nr}}(V = 0)$. With these assumptions, Eq. 14 can be rewritten as:

$$J(V, E_g) = q\left[\frac{\dot{N}_{\text{emit}}(E_g, V, T_{\text{skin}}) - \dot{N}_{\text{emit}}(E_g, 0, T_{\text{skin}})}{\eta_{\text{ext}}} - \dot{N}_{\text{abs}}(E_g) + \dot{N}_{\text{emit}}(E_g, V, T_{\text{skin}})\right] \tag{16}$$

which is used to obtain power densities where $\eta_{\text{ext}} < 100\%$. As highlighted by Pusch et al.[8], this expression yields an approximately linear relationship between η_{ext} and max power density for blackbody environments. The linearity is even more notable where downwelling radiation is significant, as is the case for the conditions modelled in this work. Ono et al.[3] directly assume a linear relationship between η_{ext} and generated power when accounting for non-radiative processes, which if applied here would yield very similar results.

Sensitivity to finite spectral range

The modelled downwelling radiance was confirmed to extend to large enough wavenumbers/photon energies to accurately calculate the detailed balance power outputs for the bandgaps up to 0.3 eV reported in this work. In order to do this, the downwelling photon flux density beyond the modelled range was bounded using two scenarios: in the first, the downwelling beyond the modelled range is set to a blackbody emission at T_{skin}. This is an upper bound on the downwelling. In the lower bound, the downwelling is set to 0 beyond the modelled range.

Over the 0.05 to 0.3 eV bandgaps reported in this work, for the 'Telfer low' conditions, there is at most a 1.8×10^{-7} W.m^{-2} difference between the bounding estimates, which corresponds to about 0.0006% of the calculated power output. The results are comparable for other conditions modelled. The uncertainty from the finite spectral range (up to 5500 cm−1 / 0.0682 eV, which replaces the upper bound of ∞ in Eq. 6) of the atmospheric modelling is therefore negligible. Figure S4 of the supplemental shows the high and low bounding downwelling flux estimates and the difference between the two resulting power density curves.

Optimization

The Python library pygmo2 was used for optimization, where the pygmo interface acts as a wrapper for a simple Powell method implemented in the library SciPy. The Powell method as implemented in SciPy was used to optimize over V to obtain the max power points in all plots where power is reported, and to optimize over E_g and V simultaneously, as shown in Figure 3.

Solar PV average power density

In order to compare the power densities calculated for terrestrial TRDs to solar PV, a reference solar power density was calculated and plotted in Figure 6. Using NREL's PVWatts calculator for Sydney, with a standard 19% efficient module and default settings, gives an annual yield of 1499 kWh/kW$_{\mathrm{p}}$. A 19% efficient module under STC (1000 W.m^{-2} irradiance) would produce 190 W.m^{-2} (so a rated power output of 0.19 kW$_{\mathrm{p}}$.m^{-2}).

The yearly average power density for 19% efficient module in Sydney is estimated as follows:

$$\text{energy density per year} = 0.19\ \mathrm{kW_p.m^{-2}} \times 1499\ \mathrm{kWh/kW_p} = 284.81\ \mathrm{kWh.m^{-2}} \tag{17}$$

$$\text{energy density per day} = \frac{\text{energy density per year}}{\text{days per year}} = \frac{284.81\ \mathrm{kWh.m^{-2}}}{365} = 780.301\ \mathrm{Wh.m^{-2}} \tag{18}$$

$$\text{average power density} = \frac{780.301\ \mathrm{Wh.m^{-2}}}{24\ \mathrm{h}} = 32.51\ \mathrm{W.m^{-2}} \tag{19}$$

This yearly average power density is comparable to the 1 kWh.m^{-2} production per day estimate used by Deppe and Munday[7] and the 29 W.m^{-2} for a 17% efficient module estimate used by Strandberg[6].

Quantification and statistical analysis

There are no quantification or statistical analyses to include in this study.

References

1. Byrnes, S. J., Blanchard, R., and Capasso, F. (2014). Harvesting renewable energy from Earth's mid-infrared emissions. Proc. Natl. Acad. Sci. U.S.A. 111, 3927–3932. https://pnas.org/doi/full/10.1073/pnas.1402036111. doi:10.1073/pnas.1402036111.

2. Santhanam, P., and Fan, S. (2016). Thermal-to-electrical energy conversion by diodes under negative illumination. Phys. Rev. B 93, 161410. https://link.aps.org/doi/10.1103/PhysRevB.93.161410. doi:10.1103/PhysRevB.93.161410. Publisher: American Physical Society.

3. Ono, M., Santhanam, P., Li, W., Zhao, B., and Fan, S. (2019). Experimental demonstration of energy harvesting from the sky using the negative illumination effect of a semiconductor photodiode. Applied Physics Letters 114, 161102. https://pubs.aip.org/apl/article/114/16/161102/37120/Experimental-demonstration-of-energy-harvesting. doi:10.1063/1.5089783.

4. Nielsen, M. P., Pusch, A., Sazzad, M. H., Pearce, P. M., Reece, P. J., and Ekins-Daukes, N. J. (2022). Thermoradiative Power Conversion from HgCdTe Photodiodes and Their Current–Voltage Characteristics. ACS Photonics 9, 1535–1540. https://doi.org/10.1021/acsphotonics.2c00223. doi:10.1021/acsphotonics.2c00223. Publisher: American Chemical Society.

5. Nielsen, M. P., Pusch, A., Pearce, P. M., Sazzad, M. H., Reece, P. J., Green, M. A., and Ekins-Daukes, N. J. (2024). Semiconductor thermoradiative power conversion. Nature Photonics. https://doi.org/10.1038/s41566-024-01537-5. doi:10.1038/s41566-024-01537-5.

6. Strandberg, R. (2015). Theoretical efficiency limits for thermoradiative energy conversion. Journal of Applied Physics 117, 055105. https://pubs.aip.org/jap/article/117/5/055105/383865/Theoretical-efficiency-limits-for-thermoradiative. doi:10.1063/1.4907392.

7. Deppe, T., and Munday, J. N. (2020). Nighttime Photovoltaic Cells: Electrical Power Generation by Optically Coupling with Deep Space. ACS Photonics 7, 1–9. https://doi.org/10.1021/acsphotonics.9b00679. doi:10.1021/acsphotonics.9b00679. Publisher: American Chemical Society.

8. Pusch, A., Gordon, J. M., Mellor, A., Krich, J. J., and Ekins-Daukes, N. J. (2019). Fundamental Efficiency Bounds for the Conversion of a Radiative Heat Engine's Own Emission into Work. Phys. Rev. Appl. 12, 064018. https://link.aps.org/doi/10.1103/PhysRevApplied.12.064018. doi:10.1103/PhysRevApplied.12.064018. Publisher: American Physical Society.

9. Phillips, J. D. (2022). Evaluation of Auger Limited Behavior in Thermoradiative Cells. 2022 IEEE 49th Photovoltaics Specialists Conference (PVSC) (0009–0011). doi:10.1109/PVSC48317.2022.9938669.

10. Vurgaftman, I., and Meyer, J. R. (2023). Simple model of power generation in thermoradiative devices including realistic nonradiative processes. APL Energy 1, 036111. https://doi.org/10.1063/5.0181036. doi:10.1063/5.0181036.

11. Hersbach, H., Bell, B., Berrisford, P., Hirahara, S., Horányi, A., Muñoz-Sabater, J., Nicolas, J., Peubey, C., Radu, R., Schepers, D., Simmons, A., Soci, C., Abdalla, S., Abellan, X., Balsamo, G., Bechtold, P., Biavati, G., Bidlot, J., Bonavita, M., De Chiara, G., Dahlgren, P., Dee, D., Diamantakis, M., Dragani, R., Flemming, J., Forbes, R., Fuentes, M., Geer, A., Haimberger, L., Healy, S., Hogan, R. J., Hólm, E., Janisková, M., Keeley, S., Laloyaux, P., Lopez, P., Lupu, C., Radnoti, G., de Rosnay, P., Rozum, I., Vamborg, F., Villaume, S., and Thépaut, J.-N. (2020). The ERA5 global reanalysis. Quarterly Journal of the Royal Meteorological Society 146, 1999–2049. https://doi.org/10.1002/qj.3803. doi:10.1002/qj.3803. Publisher: John Wiley & Sons, Ltd.

12. Clough, S., Shephard, M., Mlawer, E., Delamere, J., Iacono, M., Cady-Pereira, K., Boukabara, S., and Brown, P. (2005). Atmospheric radiative transfer modeling: a summary of the AER codes. Journal of Quantitative Spectroscopy and Radiative Transfer 91, 233–244. https://www.sciencedirect.com/science/article/pii/S0022407304002158. doi:10.1016/j.jqsrt.2004.05.058.

13. Ausgrid average electricty consumption by LGA FY2023 pdf (2023). https://www.ausgrid.com.au/Industry/Our-Research/Data-to-share/Average-electricity-use.

14. Cady-Pereira, K., Alvarado, M., Mlawer, E., Iacono, M., Delamere, J., and Pernak, R. AER Line File Parameters (2020). doi:10.5281/zenodo.3837549.

15. Anderson, G. P., Clough, S. A., Kneizys, F. X., Chetwynd, J. H., and Shettle, E. P. AFGL (Air Force Geophysical Laboratory) Atmospheric Constituent Profiles (0-120km). Technical Report ADA175173 Air Force Geophysics Lab Hanscom AFB, MA, USA (1986).

16. Harrison, J. jamieh8/TRD_atmospheric_calc: v1.0.0 (2024). https://doi.org/10.5281/zenodo.12199944. doi:10.5281/zenodo.12199944.

17. Mlawer, E., Cady-Pereira, K., Mascio, J., and Gordon, I. (2023). The inclusion of the MT_ckd water vapor continuum model in the HITRAN molecular spectroscopic database. Journal of Quantitative Spectroscopy and Radiative Transfer 306, 108645. https://www.sciencedirect.com/science/article/pii/S0022407323001632. doi:10.1016/j.jqsrt.2023.108645.

18. Gordon, I., Rothman, L., Hill, C., Kochanov, R., Tan, Y., Bernath, P., Birk, M., Boudon, V., Campargue, A., Chance, K., Drouin, B., Flaud, J.-M., Gamache, R., Hodges, J., Jacquemart, D., Perevalov, V., Perrin, A., Shine, K., Smith, M.-A., Tennyson, J., Toon, G., Tran, H., Tyuterev, V., Barbe, A., Császár, A., Devi, V., Furtenbacher, T., Harrison, J., Hartmann, J.-M., Jolly, A., Johnson, T., Karman, T., Kleiner, I., Kyuberis, A., Loos, J., Lyulin, O., Massie, S., Mikhailenko, S., Moazzen-Ahmadi, N., Müller, H., Naumenko, O., Nikitin, A., Polyansky, O., Rey, M., Rotger, M., Sharpe, S., Sung, K., Starikova, E., Tashkun, S., Auwera, J. V., Wagner, G., Wilzewski, J., Wcisło, P., Yu, S., and Zak, E. (2017). The HITRAN2016 molecular spectroscopic database. Journal of Quantitative Spectroscopy and Radiative Transfer 203, 3–69. https://www.sciencedirect.com/science/article/pii/S0022407317301073. doi:10.1016/j.jqsrt.2017.06.038.

19. Gordon, I., Rothman, L., Hargreaves, R., Hashemi, R., Karlovets, E., Skinner, F., Conway, E., Hill, C., Kochanov, R., Tan, Y., Wcisło, P., Finenko, A., Nelson, K., Bernath, P., Birk, M., Boudon, V., Campargue, A., Chance, K., Coustenis, A., Drouin, B., Flaud, J., Gamache, R., Hodges, J., Jacquemart, D., Mlawer, E., Nikitin, A., Perevalov, V., Rotger, M., Tennyson, J., Toon, G., Tran, H., Tyuterev, V., Adkins, E., Baker, A., Barbe, A., Canè, E., Császár, A., Dudaryonok, A., Egorov, O., Fleisher, A., Fleurbaey, H., Foltynowicz, A., Furtenbacher, T., Harrison, J., Hartmann, J., Horneman, V., Huang, X., Karman, T., Karns, J., Kassi, S., Kleiner, I., Kofman, V., Kwabia–Tchana, F., Lavrentieva, N., Lee, T., Long, D., Lukashevskaya, A., Lyulin, O., Makhnev, V., Matt, W., Massie, S., Melosso, M., Mikhailenko, S., Mondelain, D., Müller, H., Naumenko, O., Perrin, A., Polyansky, O., Raddaoui, E., Raston, P., Reed, Z., Rey, M., Richard, C., Tóbiás, R., Sadiek, I., Schwenke, D., Starikova, E., Sung, K., Tamassia, F., Tashkun, S., Vander Auwera, J., Vasilenko, I., Vigasin, A., Villanueva, G., Vispoel, B., Wagner, G., Yachmenev, A., and Yurchenko, S. (2022). The HITRAN2020 molecular spectroscopic database. Journal of Quantitative Spectroscopy and Radiative Transfer 277, 107949. https://www.sciencedirect.com/science/article/pii/S0022407321004416. doi:10.1016/j.jqsrt.2021.107949.

20. Minzner, R. A. (1977). The 1976 Standard Atmosphere and its relationship to earlier standards. Reviews of Geophysics 15, 375–384. https://doi.org/10.1029/RG015i003p00375. doi:10.1029/RG015i003p00375. Publisher: John Wiley & Sons, Ltd.

Table 1: Atmospheric conditions modelled for this work

Location	Date	TCWV [mm]	Skin Temp [K]	Tag
21.75°N, 122.25°E (Telfer, Australia ●)	17-Aug-2018	6.63	301.562	Telfer low
	25-Feb-2018	34.45	306.426	Telfer mid
	18-Feb-2018	70.51	299.859	Telfer high
36.75°N, 120°W (Fresno, USA ■)	20-Feb-2018	5.32	276.298	Fres. low
	4-Jul-2018	17.21	295.680	Fres. mid
	21-Jul-2018	40.32	299.231	Fres. high
22.75°N, 5.5°E (Tamanrasset, Algeria ▲)	18-Dec-2018	2.87	287.306	Tam. low
	30-May-2018	19.97	301.828	Tam. mid
	10-Aug-2018	37.91	299.096	Tam. high
Space / 3K blackbody ★		N/A	300	3K BB

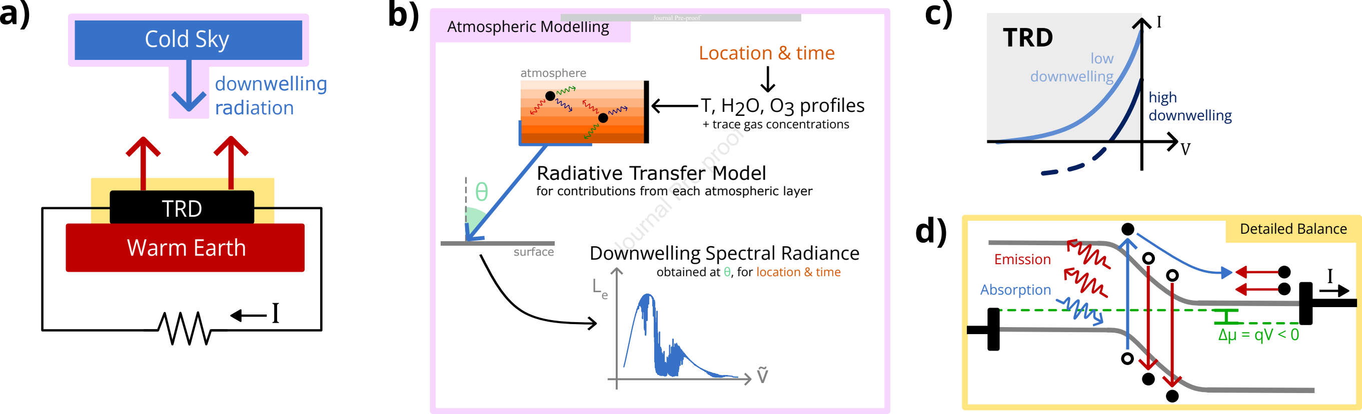

a)
Cold Sky
downwelling
radiation
TRD
Warm Earth
I
b)
Atmospheric Modelling
Location & time
atmosphere
T, H2O, O3 profiles
+ trace gas concentrations
Radiative Transfer Model
for contributions from each atmospheric layer
θ
surface
Downwelling Spectral Radiance
obtained at θ, for location & time
Le
ν̃
c)
TRD
I
low
downwelling
high
downwelling
V
d)
Detailed Balance
Emission
Absorption
I
Δμ = qV < 0

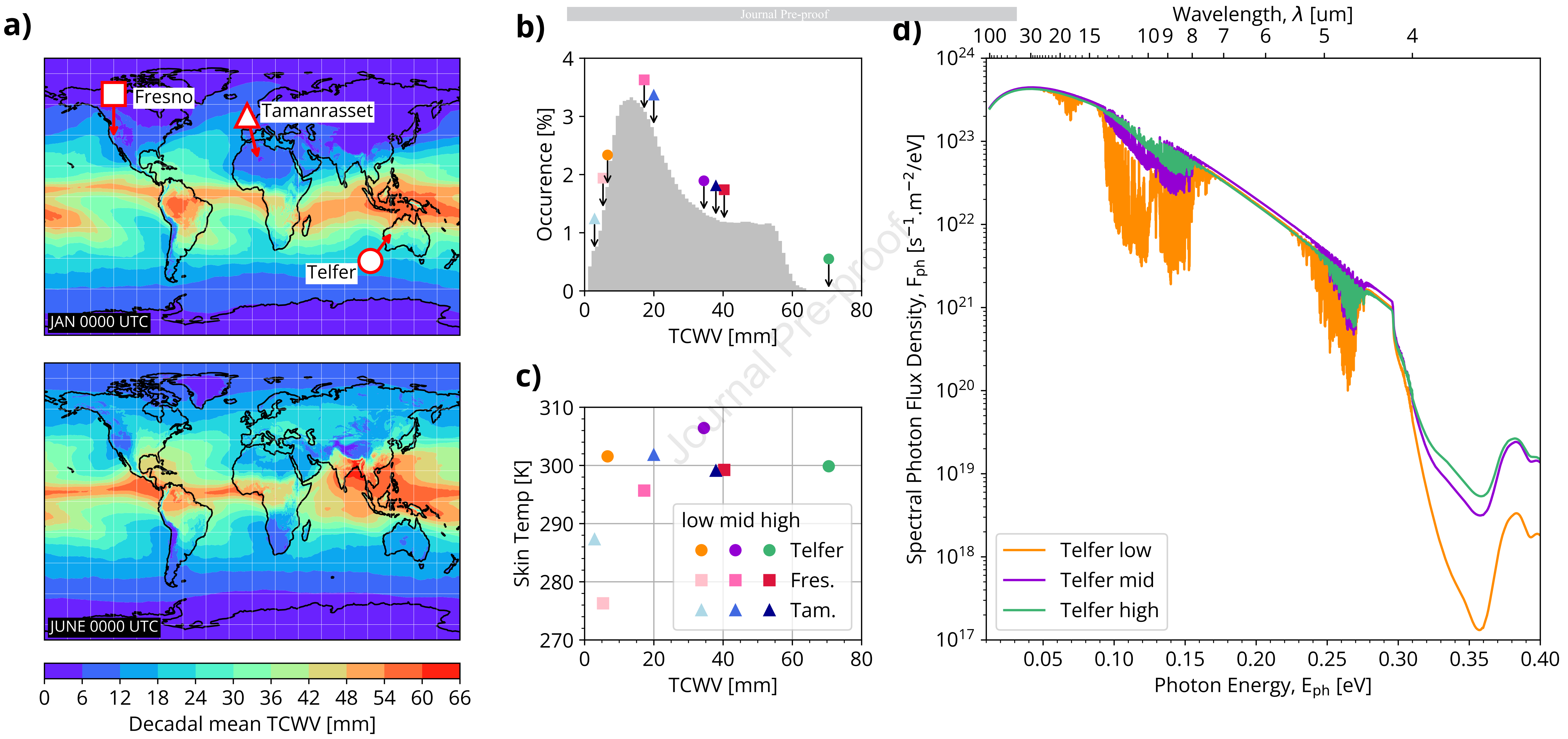
a)
Fresno
Tamanrasset
Telfer
JAN 0000 UTC
JUNE 0000 UTC
0 6 12 18 24 30 36 42 48 54 60 66
Decadal mean TCWV [mm]
b)
Occurence [%]
TCWV [mm]
c)
Skin Temp [K]
TCWV [mm]
low mid high
Telfer
Fres.
Tam.
d)
Wavelength, λ [um]
100 30 20 15 10 9 8 7 6 5 4
Spectral Photon Flux Density, F_{ph} [$s^{-1}.m^{-2}/eV$]
Photon Energy, E_{ph} [eV]
Telfer low
Telfer mid
Telfer high

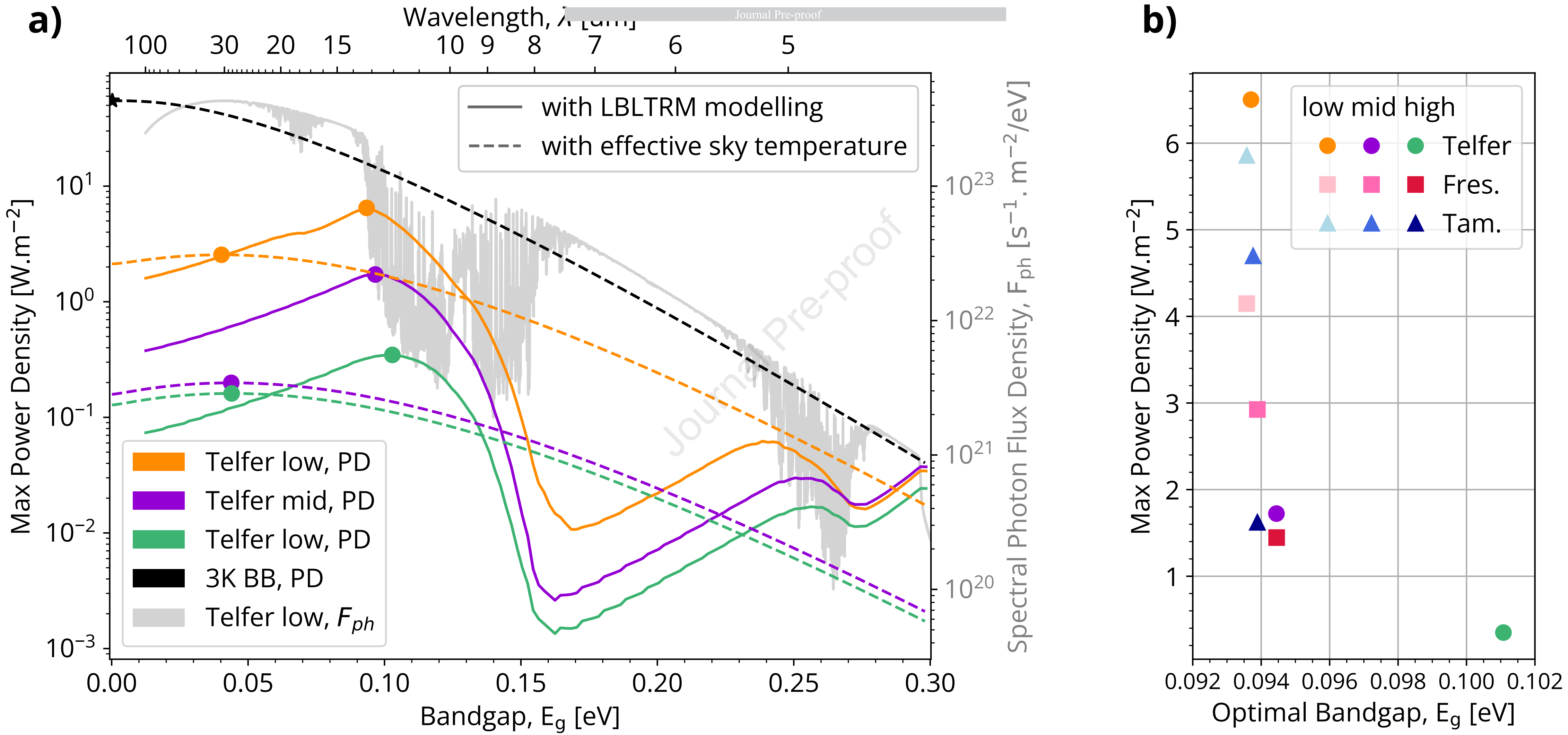
a)
Wavelength, λ [um]
100
30
20
15
10
9
8
7
6
5
with LBLTRM modelling
with effective sky temperature
Max Power Density [W.m⁻²]
Spectral Photon Flux Density, F_ph [s⁻¹.m⁻²/eV]
Telfer low, PD
Telfer mid, PD
Telfer low, PD
3K BB, PD
Telfer low, F_ph
Bandgap, E_g [eV]
0.00
0.05
0.10
0.15
0.20
0.25
0.30
b)
low mid high
Telfer
Fres.
Tam.
Max Power Density [W.m⁻²]
Optimal Bandgap, E_g [eV]
0.092
0.094
0.096
0.098
0.100
0.102

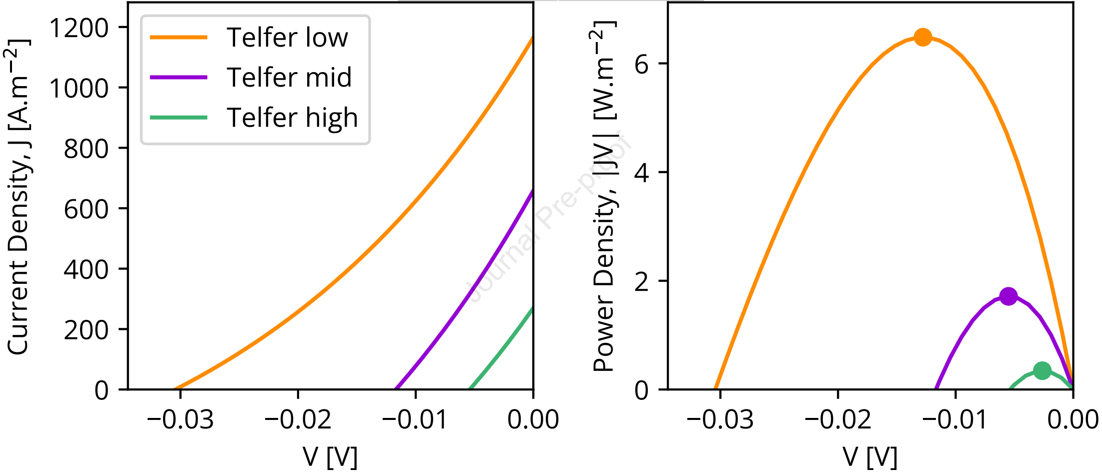
Telfer low
Telfer mid
Telfer high
Current Density, J [A.m^{-2}]
1200
1000
800
600
400
200
0
−0.03
−0.02
−0.01
0.00
V [V]
Power Density, |JV| [W.m^{-2}]
6
4
2
0
−0.03
−0.02
−0.01
0.00
V [V]

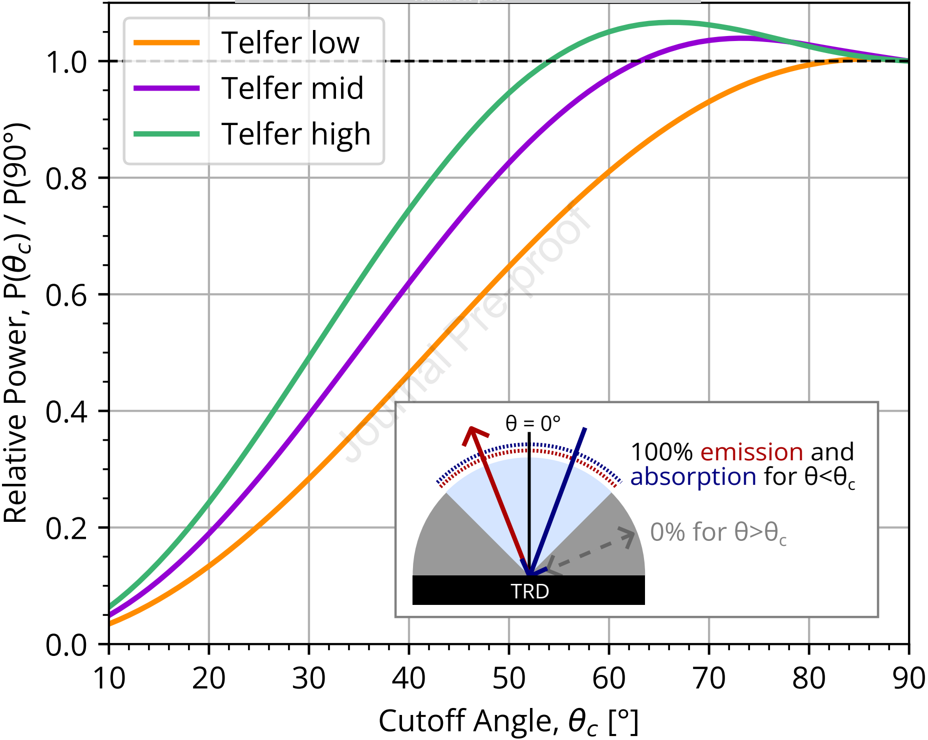
Telfer low
Telfer mid
Telfer high
Relative Power, P(θc) / P(90°)
Cutoff Angle, θc [°]
1.0
0.8
0.6
0.4
0.2
0.0
10
20
30
40
50
60
70
80
90
θ = 0°
100% emission and
absorption for θ<θc
0% for θ>θc
TRD

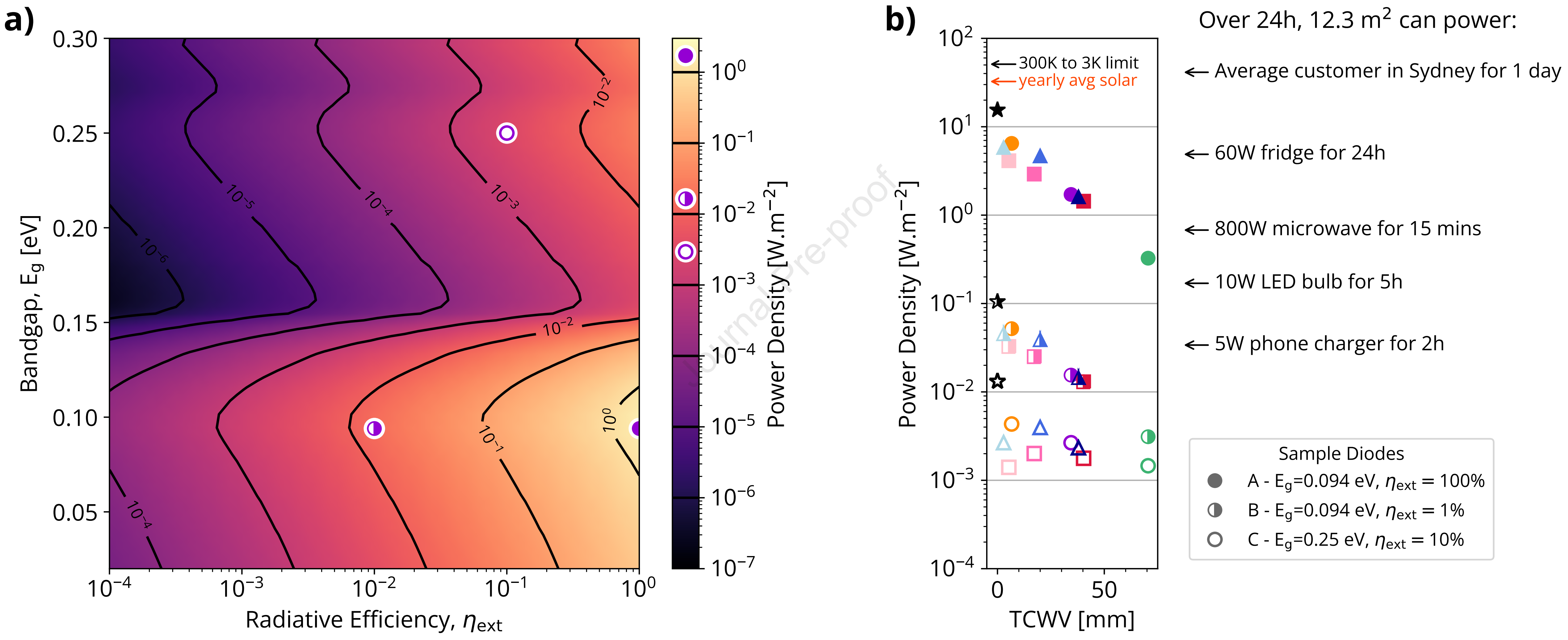
a)
Bandgap, E_g [eV]
Radiative Efficiency, η_{ext}
Power Density [W.m^{-2}]
b)
Power Density [W.m^{-2}]
TCWV [mm]
300K to 3K limit
yearly avg solar
Over 24h, 12.3 m^2 can power:
Average customer in Sydney for 1 day
60W fridge for 24h
800W microwave for 15 mins
10W LED bulb for 5h
5W phone charger for 2h
Sample Diodes
A - E_g=0.094 eV, η_{ext} = 100%
B - E_g=0.094 eV, η_{ext} = 1%
C - E_g=0.25 eV, η_{ext} = 10%

Highlights

- Thermoradiative diodes can generate power at night through thermal emission
- Power output is calculated for 9 conditions using accurate atmospheric modelling
- Power output varies with humidity, but ideal bandgap remains around 0.094 eV
- Non-radiative processes are included through non-ideal radiative efficiencies

Key resources table

REAGENT or RESOURCE	SOURCE	IDENTIFIER
Deposited data		
ERA5 dataset	Copernicus Climate Data Store (CDS)	DOI: 10.24381/cds.143582cf
US standard atmosphere	AFGL report	ADA175173
AER 3.8.1 line database (used by LBLRTM)	Open code	DOI 10.5281/zenodo.3837549
LBLRTM modelling results	Published in Zenodo archive	DOI 10.5281/zenodo.12199943
Software and algorithms		
LBLRTM code, v12.13	Open code	https://github.com/AER-RC/LBLRTM
MT_CKD model, v3.6	Open code	https://github.com/AER-RC/MT_CKD
Detailed balance code	Published in Zenodo archive	DOI 10.5281/zenodo.12199943